Laminated Monolithic Perovskite/Silicon Tandem Photovoltaics

Julie Roger, Luisa K. Schorn, Minasadat Heydarian, Ahmed Farag, Thomas Feeney, Daniel Baumann, Hang Hu, Felix Laufer, Weiyuan Duan, Kaining Ding, Andreas Lambertz, Paul Fassl, Matthias Worgull, and Ulrich W. Paetzold*

Perovskite/silicon tandem photovoltaics have attracted enormous attention in science and technology over recent years. In order to improve the performance and stability of the technology, new materials and processes need to be investigated. However, the established sequential layer deposition methods severely limit the choice of materials and accessible device architectures. In response, a novel lamination process that increases the degree of freedom in processing the top perovskite solar cell (PSC) is proposed. The very first prototypes of laminated monolithic perovskite/silicon tandem solar cells with stable power output efficiencies of up to 20.0% are presented. Moreover, laminated single-junction PSCs are on par with standard sequential layer deposition processed devices in the same architecture. The numerous advantages of the lamination process are highlighted, in particular the opportunities to engineer the perovskite morphology, which leads to a reduction of non-radiative recombination losses and and an enhancement in open-circuit voltage (V_{oc}). Laminated PSCs exhibit improved stability by retaining their initial efficiency after 1-year aging and show good thermal stability under prolonged illumination at 80 °C. This lamination approach enables the research of new architectures for perovskite-based photovoltaics and paves a new route for processing monolithic tandem solar cells even with a scalable lamination process.

1. Introduction

Over the past decade, the power conversion efficiency (PCE) of perovskite photovoltaics has steadily increased. Today, single-junction PSC achieve outstanding performances exceeding 25%.[1] The unique optoelectronic properties of perovskite materials, especially long diffusion length,[2,3] short absorption length,[4] and bandgap tunability over a wide range of energies[5–8] make this technology an ideal candidate for tandem applications. Of particular interest are monolithic perovskite/silicon tandem photovoltaics.[9] By processing top PSCs over

silicon bottom solar cells, PCEs exceeding the record of single-junction silicon solar cells have been demonstrated in 2018.[10–12] Thereby, the perovskite/silicon tandem technology promises to reduce the levelized cost of electricity of the market-dominating silicon photovoltaics.[13] Recently, Al-Ashouri et al. reported the current record for a perovskite/silicon tandem solar cell with a monolithic device exhibiting more than 29% PCE and highlighted the route for improvement of PCEs to beyond 30%.[14]

Suitable choice of optimal charge transport, absorber, and electrode materials in the top PSC is of highest relevance to maximize the PCE and stability of monolithic tandem photovoltaics. In particular, the device architecture needs to be optimized to enable improved current matching,[15,16] reduced parasitic absorption,[17,18] and maximized charge carrier extraction.[19–21] However, the standard sequential layer deposition method significantly limits the choice of materials and compatible processing techniques, since each material deposition must preserve the already processed layer stack. There are numerous reasons to consider a deposition technique incompatible. Some inherently damage the underlying layers, as is the case for physical vapor deposition.[22] Others require temperatures exceeding the thermal budget of preceding layers, for example, 200 °C for silicon heterojunction (SHJ) solar cells.[23]

The sequential layer deposition of conventional PSC fabrication implies critical constraints to the device architectures.[24,25] Given the low durability of the perovskite semiconductor thin films toward diffusion of metals, plasma treatment, polar

---

J. Roger, L. K. Schorn, A. Farag, H. Hu, P. Fassl, M. Worgull, U. W. Paetzold
Institute of Microstructure Technology
Karlsruhe Institute of Technology (KIT)
Hermann-von-Helmholtz-Platz 1, 76344 Karlsruhe, Germany
E-mail: ulrich.paetzold@kit.edu

M. Heydarian, T. Feeney, D. Baumann, H. Hu, F. Laufer, P. Fassl, U. W. Paetzold
Light Technology Institute
Karlsruhe Institute of Technology (KIT)
Engesserstrasse 13, 76131 Karlsruhe, Germany
W. Duan, K. Ding, A. Lambertz
Institute of Energy and Climate Research
IEK-5 Photovoltaics
Forschungszentrum Jülich GmbH
52428 Jülich, Germany

**ADVANCED
SCIENCE NEWS**
www.advancedsciencenews.com

**ADVANCED
ENERGY
MATERIALS**
www.advenergymat.de

solvents, or high temperatures, the range of accessible processes and materials that can be deposited on top are subject to severe compromises. For example, due to the low stability of the perovskite absorber layer toward argon plasma, sputtered charge transport layers, and transparent conducting oxides (TCOs) such as nickel oxide (NiO_x) and indium tin oxide (ITO), respectively, cannot be processed directly on top of perovskite semiconductor.[26,27] In response, alternative fabrication routes have been investigated for single-junction PSCs and perovskite-based tandem solar cells to increase the degree of freedom in the device architecture.[24,28–31] Prominent examples are mechanically-stacked devices (e.g., using transparent conductive adhesives (TCAs), also referred to as e-glue) to bond two separate half-stacks or top- and bottom solar cells in a tandem solar cell.[28,29,32–40] Perovskite/silicon monolithic tandem solar cells using TCAs exhibit up to 21% PCE,[32,40] and a recent simple superposition technique, in which the back electrode of the PSC is brought into contact with the front contact of the silicon bottom solar cell, enabled PCEs of over 26%.[41,42] In contrast to these mechanically-stacking processes, Dunfield et al. in 2018,[24] Schmager et al.,[31] and Yang et al.,[43] reported on the lamination of single-junction PSCs via hot-pressing of two separate perovskite device half-stacks.[31] These process conditions (high temperatures up to 200 °C, pressures up to 800 bar) enable the recrystallization of the perovskite thin film during lamination, thereby uniting the half-stacks. Such laminated PSCs demonstrated PCEs of up to 14.6%.[31] We note that this complete device lamination method is different to simple recrystallization of single perovskite films via hot-pressing,[39] or hot-pressing sublimation.[44] While these approaches can improve the quality of the perovskite films, the top device stack is still fabricated using the standard sequential layer deposition method.

Here, we propose a novel lamination process to overcome the aforementioned limitations related to the standard sequential layer deposition method and open a new route to fabricate monolithic tandem perovskite/silicon solar cells. The laminated tandem device consists of two independently produced half-stacks hot-pressed together. The combination of heat and pressure promotes perovskite recrystallization, thus creating an intimate contact at the interface. In our previous work,[31] we investigated the multiple advantages of this technique for single-junction PSCs. In particular, via the separate deposition of charge transport layers, the degree of freedom in choice of materials—including electrodes and substrates—is substantially increased. In addition, the perovskite can be processed on top of either or even both half-stacks, providing further freedom in the layer sequence and material combination. Thus, this lamination technique enables new architectures that otherwise would either be impossible or prohibitively difficult to fabricate.

We present the first prototypes of monolithic perovskite/silicon tandem solar cells produced by this lamination approach, with a PCE of up to 20%. We attribute this achievement to the optimization of our lamination process to be competitive with the standard sequential layer deposition method. In fact, we demonstrate laminated single-junction PSCs that are comparable to reference sequentially deposited devices, exhibiting PCEs of up to 17.5%. We show that the high pressure (80 MPa) and temperature (90 °C) applied during lamination

appear to be beneficial to the perovskite morphology, which exhibits reduced roughness and larger grains, thereby reducing non-radiative recombination losses. The improved perovskite morphology is accompanied by enhanced shelf-stability of the laminated devices after 1-year aging. Finally, laminated PSCs show good thermal stability under continuous illumination over 100 h while heated at 80 °C.

2. Results and Discussion

2.1. Prototype Laminated Monolithic Perovskite/Silicon Tandem Solar Cells

The lamination process in focus of this study allows combining two separate half-stacks of a PSC by recrystallizing the perovskite thin film at elevated temperatures and high pressures.[31] Prototype monolithic perovskite/silicon tandem solar cells are fabricated by laminating stack A: the front layer stack of an n-i-p PSC on stack B: a modified SHJ bottom solar cell (see **Figure 1**a). Stack A comprises a flexible polyethylen naphthalat (PEN) foil superstrate coated with a transparent conductive ITO electrode (300 nm), a double layer electron transport layer of tin oxide (SnO_x; ≈35 nm) and fullerene C60 (20 nm). Stack B denotes a double-side-polished SHJ bottom solar cell in the architecture: a-Si:H<n>/a-Si:H<i>/c-Si wafer <n>/a-Si:H<i>/a-Si:H<p> covered with a thin ITO recombination layer (30 nm), and a double hole transport layer of sputtered NiO_x (20 nm) and a self-assembled monolayer of [2-(9H-carbazol-9-yl)ethyl]phosphonic acid; 2PACz). The triple cation $Cs_{0.1}(MA_{0.17}FA_{0.83})_{0.9}Pb(I_{0.83}Br_{0.17})_3$ perovskite that is recrystallized during the lamination step is processed on top of stack B (see Experimental Section for details on processing conditions). In our preceding study on laminated single-junction PSCs, we demonstrated the compatibility of this perovskite composition with the demanding conditions of the lamination process, providing robust and stable performance.[31,45] The lamination process requires elevated pressures (80 MPa) and a temperature of 90 °C for a duration of 5 min. As a consequence of this lamination step, the perovskite thin film recrystallizes and unites both half-stacks into a monolithic perovskite/silicon tandem solar cell.

First, we demonstrate the successful realization of perovskite/silicon tandem solar cells by means of lamination with a champion PCE of 20.0% (see Figure 1b), exceeding the PCE of the champion laminated single-junction semi-transparent (ST) PSC, which will be presented later, by 30%$_{rel}$. The current density–voltage ($J–V$) characteristics of the champion device exhibits a fill factor (FF) of 73.6%, a short-circuit current density (J_{sc}) of 15.5 mA cm^{-2}, an (V_{oc}) of 1.75 V, and minor hysteresis. As expected in a monolithic tandem device, the V_{oc} of the tandem solar cell nears the sum of the voltage of both sub-cells. The reproducibility of our lamination approach is highlighted by high performances for the five best laminated tandem devices, which achieved a V_{oc} of ≈1.75 V on average (in Figure S1, Supporting Information). The simple optical and electrical system of our prototypes already yield comparable V_{oc} to reported values for monolithic perovskite/silicon tandem solar cells fabricated by mechanical stacking.[32,42,46,47] Furthermore, the champion device demonstrates a stabilized
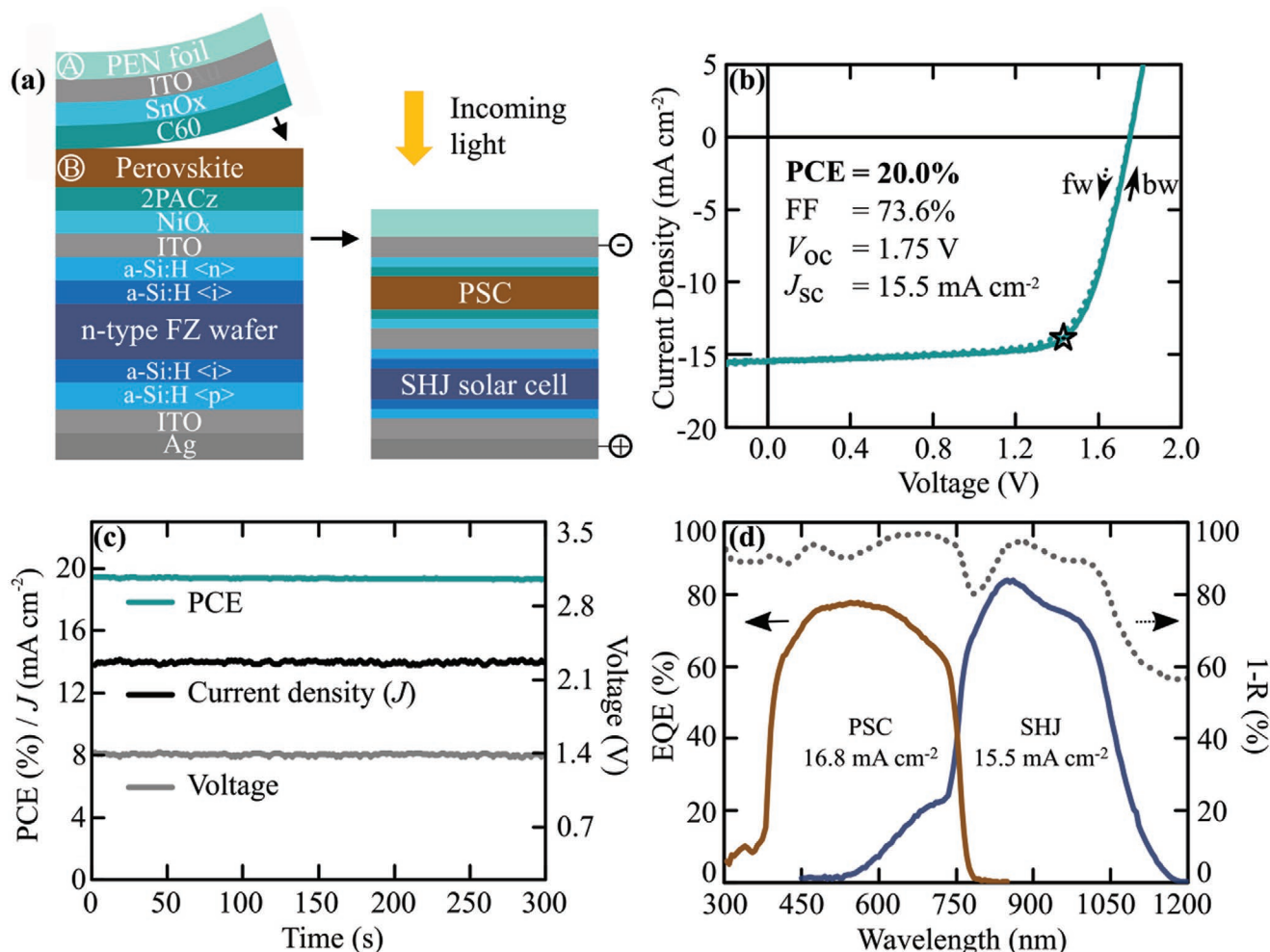
Figure 1. a) Illustration of the lamination process and device architecture of the laminated monolithic perovskite/silicon tandem solar cells. Stack A uses a flexible PEN superstrate and stack B builds on a rigid SHJ bottom solar cell. The lamination of these two half-stacks is performed at a temperature of 90 °C under a pressure of 80 MPa for 5 min. b) $J–V$ characteristics of the champion device, including the PCE, FF, J_{sc}, and V_{oc}. The star indicates the maximum power point in backward scan direction (1.43 V; 13.9 mA cm^{-2}). c) Stabilized maximum power point (MPP) tracking showing PCE, current density, and voltage over time. d) EQE of the champion device. Corresponding current densities for AM 1.5 G irradiation generated in the perovskite and SHJ sub-cells are shown in the respective areas. A reflectance (R) measurement from an identical layer stack is also displayed. More statistics for laminated tandem solar cells are provided in Figure S1, Supporting Information.

PCE of 19.3% (see Figure 1c). Despite high temperature and pressure applied during the lamination process, the perovskite absorber layer is of high quality and no severe degradation is expected. Laminated tandem devices exhibit some uncertainty in their exact active area, as minute changes in alignment can modify the overlap in active area of the top and bottom half-stacks, which are not guaranteed clearly defined edges due to minor processing differences. Therefore, the J_{sc} of the top PSC (16.8 mA cm^{-2}) and the SHJ bottom solar cell (15.5 mA cm^{-2}) are determined by external quantum efficiency (EQE) measurements, indicating further improvements are possible with regards to current matching (see Figure 1d). Note that a layer of magnesium fluoride (MgF$_2$; 125 nm) is applied on the front side of the tandem device and serves as an anti-reflective layer to enhance light incoupling (see Figure S2, Supporting Information). Despite this, the J_{sc} of our laminated perovskite/silicon tandem is lower compared to record tandem devices

reported in literature (≈19.5–20 mA cm^{-2}),[48–50] which is due to significant parasitic absorption losses in the 125 µm thick PEN foil and the sputtered 300 nm thick ITO front electrode. These layers reduce the transmittance to below 20% in the wavelength range of 300 to 380 nm and below 85% at longer wavelengths (see Figure S3, Supporting Information). Strategies to reduce these losses in the future are i) replacing the PEN foil with a more transparent superstrate such as glass and ii) employing more transparent front TCOs, for example, hydrogen-doped indium oxide (IO:H) or high temperature processed indium zinc oxide (IZO).[51] In addition, the SHJ solar cell used in this work is polished on both sides, therefore, imperfect light incoupling is expected on its front and rear sides, which is apparent in the reflectance measurement at around 790 nm and at wavelengths longer than 1000 nm, respectively (see Figure 1c). The use of both-side textured silicon solar cells—which are standard for silicon photovoltaics—would significantly reduce

**ADVANCED
SCIENCE NEWS**

www.advancedsciencenews.com

**ADVANCED
ENERGY
MATERIALS**

www.advenergymat.de

these reflection losses and improve light trapping.[19,52–54] While it is challenging to cover conventional front-side textures of silicon substrates with pyramidal dimensions of ≈5 µm via spin-coating, recent studies indicate the possibility to realize enclosed films on adapted silicon solar cells textures (dimensions ≈1–2 µm) with particularly thick perovskite layers,[55–57] or on nanotextured silicon substrates.[58] Making use of such techniques, the lamination approach introduced in this work is expected to be compatible with textured silicon bottom solar cells. Further potential advancements to improve the J_{sc} would be optimization of the perovskite thickness according to its bandgap energy, which was previously reported increases generated energy yield.[15,21,59,60] In addition, since the current of the laminated tandem devices is slightly limited by the SHJ bottom solar cell (see Figure 1d), the current matching could be further improved by increasing the perovskite bandgap of the top PSC.[14,57] The bandgap of the triple-cation perovskite absorber employed in this work is ≈1.64 eV, as determined from the inflection point of the EQE.[61] Ultimately, through the successful fabrication of monolithic perovskite/silicon tandem devices, we demonstrate that lamination is readily applicable to the field of tandem photovoltaics. This approach offers new freedom in the choice of materials and can be used to explore new architectures and combinations of different technologies, such as all-perovskite and perovskite/copper indium gallium selenide tandem solar cells.[5,62–64] In addition, parallel manufacturing of cells, freedom in the choice of layer deposition processes and compatibility with large-scale production methods such as roll-to-roll, make this versatile lamination process particularly promising for future industrial application.

2.2. Lamination versus Sequential Layer Deposition and Laminated Semi-Transparent Perovskite Solar Cells

The above presented successful realization of a laminated perovskite/silicon tandem solar cell by recrystallization of the perovskite layer builds on an improvement in our lamination process and the development of durable laminated ST PSCs. In fact, we demonstrate laminated PSCs that are on par with reference devices processed by sequential layer deposition. In order to allow for a direct comparison, both PSCs are fabricated using the same p-i-n architecture (see **Figure 2**a). The bottom device stack is identical in both cases and consists of a glass/ITO substrate, a double hole transport layer of NiO_x (20 nm) and 2PACz, and the triple cation perovskite layer. Reference devices are completed by sequential evaporation of a C60 (20 nm) and Bathocuproine (BCP; 5 nm) double electron transport layer and an Au electrode (75 nm). For laminated devices, these materials are deposited in reverse order on a PEN foil superstrate. Afterward, the two half-stacks are laminated at the perovskite/C60 interface, yielding a functional PSC. The same lamination parameters (90 °C, 80 MPa, 5 min) are also employed for tandem devices.

We emphasize that laminated PSCs can achieve similar PCEs compared to reference devices processed with methods developed over decades (see Figure 2b). A significant statistical data of laminated solar cells are presented to assess the yield of the lamination process, which leads to ≈83% working devices, the same as for the reference devices (see Figure S4, Supporting

Information). The champion laminated opaque solar cell exhibited a PCE of 17.5%. Moreover, we demonstrate that lamination is a suitable fabrication method for ST PSCs, which are essential for tandem applications. To that end, opaque gold is replaced by a transparent 300 nm ITO electrode and BCP by 35 nm atomic layer deposition (ALD) deposited SnO_x, as shown in Figure 2c.

In addition, the best ST PSC demonstrates a PCE of 15.4% with negligible hysteresis (Figure S5, Supporting Information). This is respectively $20\%_{rel}$ and $34\%_{rel}$ higher than our previously reported values in opaque and ST configurations for a similar lamination process.[31] J–V characteristics of champion devices in each category are shown in Figure 2d. Importantly, the champion opaque laminated PSC and reference reach the same PCE, with a slightly lower FF in the laminated PSC being compensated by a higher V_{oc} and a similar J_{sc}. Furthermore, FFs of champion laminated PSCs remain comparable in opaque and ST configurations, despite the lower conductivity of ITO compared to the gold rear electrode. The PCE of the ST PSC is limited by a low J_{sc} compared to the opaque PSCs (see Figure 2e), given enhanced transmittance of photons near the bandgap (≈600–750 nm) due to imperfect light absorption. The successful demonstration of laminated ST PSCs is a milestone on the route to perovskite-based tandem photovoltaics, since we employ the same layer stack, perovskite absorber, and lamination process as in a tandem device. In particular, we observe that the obtained FFs match those of the tandem devices presented above (statistical data for ST laminated devices can be found in Figure S6, Supporting Information).

2.3. Morphology of Laminated Perovskite Thin Films

In addition to providing a versatile alternative route to fabricate perovskite-based tandem and single-junction solar cells, the lamination process allows engineering the morphology of the laminated perovskite thin film with apparent benefits for device performance. Indeed, the average V_{oc} of our laminated PSC is enhanced compared to reference devices (see Figure S7, Supporting Information). Notably, this enhancement is in good agreement with the enhancement in implied V_{oc} determined from photoluminescence quantum yield (PLQY) measurements and independent on light intensity (see **Figure 3**a). The reduced ideality factor further indicates that laminated PSCs exhibit a reduced contribution of non-radiative recombination.[65] As shown in Figure 3b, laminated perovskite thin films exhibit a reduced roughness and larger grain size after the lamination-induced recrystallization during the hot-pressing process. The root mean square (RMS) roughness of perovskite film decreases from 20.0 to 1.7 nm after lamination. Planar perovskite surfaces further exhibit less scattering which is confirmed by optical characterization of laminated PSCs that exhibit a significantly reduced diffuse reflectance. Furthermore, the grain size of perovskite increases from 284 to 350 nm ($+23\%_{rel}$) upon lamination at 90 °C (see Figure S9, Supporting Information). This effect is amplified by an even higher lamination temperature, as the perovskite grains become larger and reach up to 778 nm (472 nm on average) after lamination at 120 °C. Additional PLQY measurements on laminated perovskite stacks (as shown in Figure S8, Supporting Information)
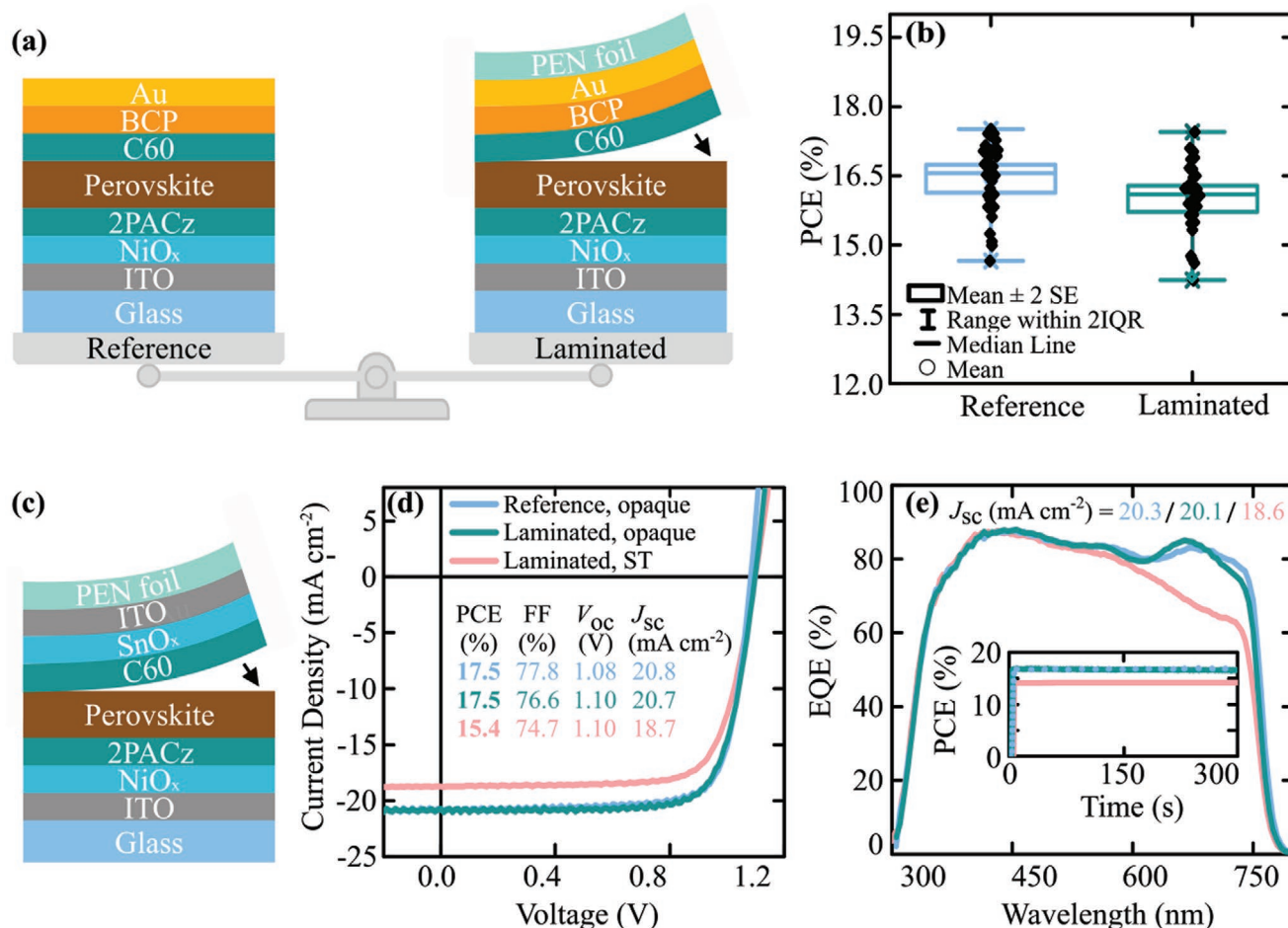
ADVANCED
SCIENCE NEWS

www.advancedsciencenews.com

ADVANCED
ENERGY
MATERIALS

www.advenergymat.de

Figure 2. a) Illustration of device architectures and lamination process, and b) PCE of opaque laminated (PSCs; x33), compared to references (x28) produced via the standard sequential layer deposition method. The arrow indicates the lamination interface between half-stacks. SE and IQR stand for standard error and interquartile range, respectively. c) Illustration of device architecture and lamination process of the laminated PSCs in ST configuration. d) Measured J–V characteristics, including the PCE, FF, J_{sc}, and V_{oc}, e) EQE and MPP tracking of champion PSCs for each category: opaque reference, opaque laminated, and ST laminated devices. The ST solar cells are illuminated from the glass side to enable a fair comparison with the opaque devices.
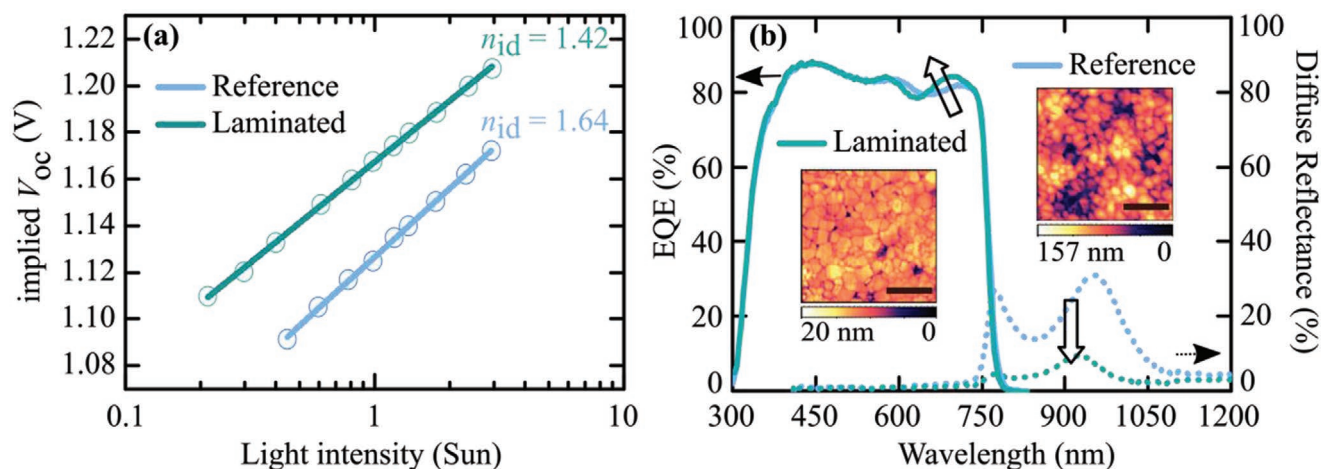

Figure 3. a) PLQY measurement showing the light intensity dependence of the implied V_{oc} for representative laminated and reference PSCs. n_{id} corresponds to the ideality factor calculated from the slope of the implied V_{oc} versus light intensity. b) EQE and diffuse reflectance of representative laminated and reference PSCs. The corresponding short-circuit current densities (J_{sc}) are 20.1 and 20.4 mA cm^{-2}, respectively. Atomic force microscopy images of laminated (left) and unpressed (right) perovskite surfaces are shown in the inset. The corresponding RMS roughness values are 20.0 (reference) and 1.7 nm (laminated). The layer stack is glass/ITO/perovskite. The colored scale indicates the height in nm and the black bar 1 μm.
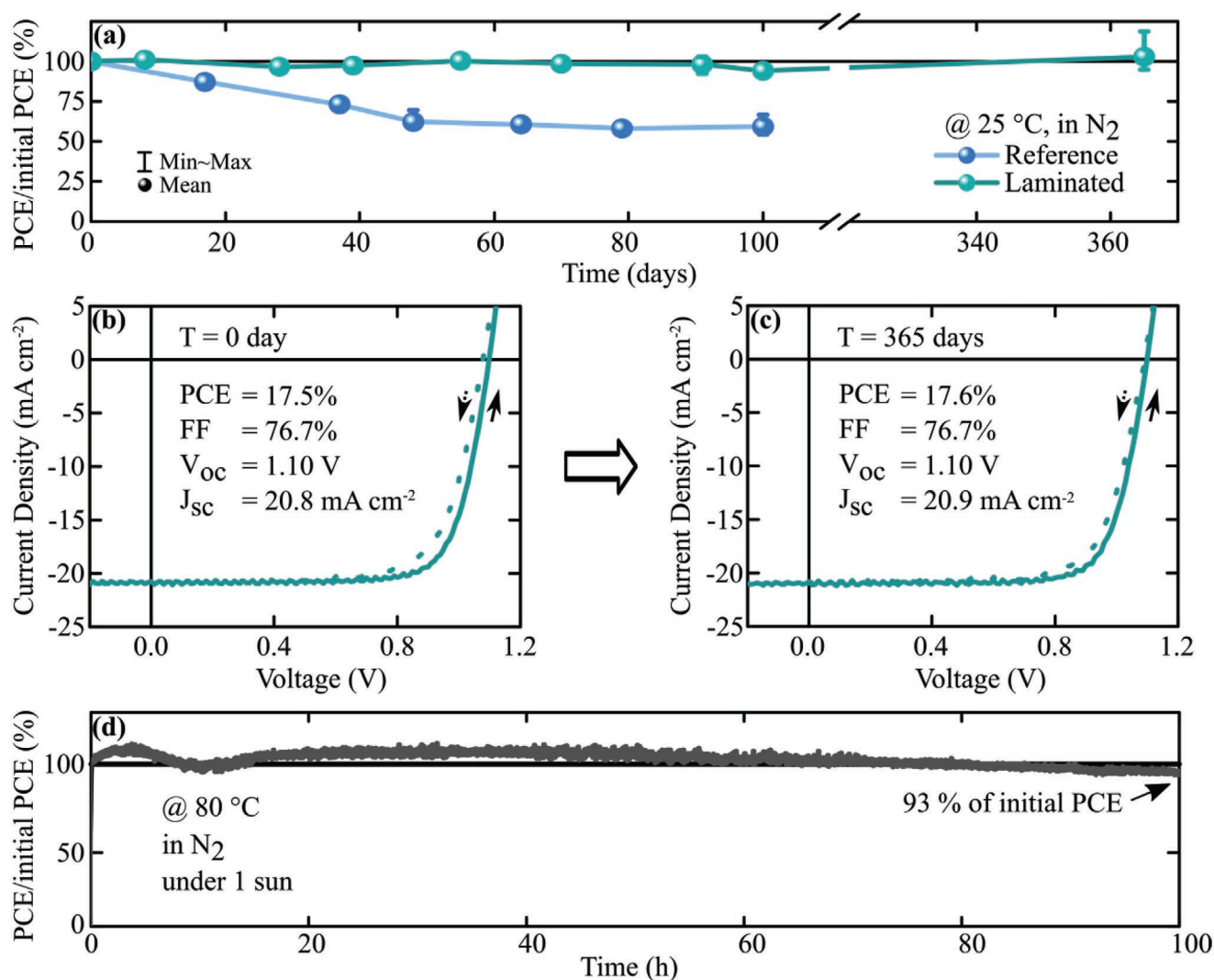
**ADVANCED
SCIENCE NEWS**
www.advancedsciencenews.com

**ADVANCED
ENERGY
MATERIALS**
www.advenergymat.de

Figure 4. a) Evolution of the PCE over 365 days compared to the initial PCE value. All devices present the opaque architecture aforementioned in Figure 2a and are stored in N_2 atmosphere in the dark and at ambient temperature (≈25 °C). Reference (PSCs; x3) and laminated PSCs (x3) are approximately bi-weekly measured during 100 days. Additionally, 10 separate laminated PSCs are measured after an aging-period of 365 days. b) J–V characteristics of the champion laminated device measured b) before ($T = 0$ day) and c) after 1-year aging ($T = 365$ days), including the PCE, FF, J_{sc}, and V_{oc}. d) MPP tracking of a representative laminated PSC over 100 h at 80 °C under continuous illumination (1 sun) in N_2 atmosphere.

provide further insights to i) highlight the differences between the perovskite/C60 interface in reference and laminated layer stacks and ii) underline the effect of perovskite recrystallization. We lay out that the lamination approach proposed in this work combines the advantages of perovskite recrystallization (larger grain size and smoother surface) and an improved perovskite/C60 interface (reduced surface area). Therewith, the improved morphology of the hot-pressed perovskite appears to play the major role in improving the V_{oc} in fully laminated PSCs.[66,67]

Additionally, the improved morphology of the perovskite layer impacts absorption near the band edge of the laminated PSC. A small shift of EQE signal appears in the wavelength range of 550 to 750 nm and can be correlated to the different roughness of the perovskite layers. This effect is emphasized by increasing the lamination time, which leads to a further decrease in RMS roughness and a stronger EQE signal shift

that perfectly mirrors the change in reflectance (Figure S10, Supporting Information). Overall, the J_{sc} is not significantly affected, on average it remains the same. Finally, although the FF of laminated PSCs is limited by a high series resistance, which may be related to the more complicated contact method due to the PEN foil, the higher shunt resistance is a further indication of the improved quality of the perovskite film by lamination (Figure S7, Supporting Information).

2.4. Improved Long-Term and Thermal Stability

Importantly, despite the harsh conditions of the hot-pressing process, laminated PSCs exhibit enhanced stability compared to references produced via sequential layer deposition. A long-term stability study (100 days, see **Figure 4**a) highlights the

improved shelf-stability of laminated PSC in nitrogen (N_2) atmosphere. While reference PSCs degrade and decrease $20\%_{rel}$ in PCE already after 30 days, laminated devices maintain their initial performance throughout the 100 days. In reference PSCs, all J–V characteristics are impacted over time and the systematic S-shape deformation reveals a reduction in charge carrier extraction (Figure S11, Supporting Information). Moreover, photoluminescence measurements illustrate the degradation in references compared to laminated PSCs (Figure S12, Supporting Information). Most important is the emergence of inhomogeneous areas in previously uniform reference PSCs, a pattern not reflected in laminated devices. One explanation of the enhanced robustness of laminated PSCs could be the improved morphology of the laminated perovskite layer. Recent studies established that larger grains and a smoother surface of the perovskite directly improve not only photovoltaics performance but also the stability of PSCs.[68–71] Furthermore, the different growth and quality of the Au electrode and thin electron transport layers in laminated PSCs could also play a role, as previously reported.[72] These layers are thermally evaporated on the smooth PEN foil and not directly onto the perovskite (as in the standard method). Therefore, critical proximity between Au and perovskite could be avoided through more continuous layers and thus limit Au migration,[73–77] providing enhanced stability for laminated PSCs. In addition, we note that the PEN foil can prevent possible leakage of volatile species under device relevant conditions, which is reported to be suppressed in encapsulated PSCs.[78,79] However, the encapsulation properties of the PEN foil require additional investigation.

It is highlighted that laminated PSCs retain their initial PCE even after a 1-year aging test. Ten of the aforementioned laminated PSCs (Figure 2b), including the five best devices, were measured before and after aging and all demonstrate very stable PCE (J–V characteristics in Figure S13, Supporting Information). The champion laminated PSC exhibits a V_{oc} of 1.10 V, a FF of 76.7%, a J_{sc} of 20.9 mA cm^{-2}, and a PCE of 17.6% (initially 17.5%) after 1-year of aging, as displayed in Figure 4b,c. While it must be taken into account that the devices were stored in N_2 atmosphere and in the dark, a stability of 1-year under these conditions still constitutes significant advance forward toward PSCs stability and future industrialization.

Finally, the combined effect of prolonged exposure to light and heat is studied. A representative laminated PSC exhibits good thermal stability under continuous illumination at 1 sun, retaining 93% of its initial PCE over 100 h at 80 °C, as displayed in Figure 4d. This thermal stability is also demonstrated by an 8-month aged laminated PSC, stored in the dark and in N_2 atmosphere. The device remains 98% of its initial PCE after operating at 80 °C under prolonged illumination over 70 h (Figure S14, Supporting Information). Since high temperatures are a critical factor in real-world outdoor conditions and accelerated degradation, the stability of laminated PSCs at 80 °C is particularly promising.

3. Conclusion

In this work, we report on a novel lamination approach to easily fabricate monolithic perovskite/silicon tandem solar cells with an increased degree of freedom for processing the top PSC architecture. In particular, we present the very first prototypes of successfully laminated tandem devices with a PCE of up to 20%. This achievement is based on the optimization of our hot-pressing process, which i) leads to laminated PSCs with PCEs of 17.5% and ii) demonstrates that lamination is competitive with the standard sequential layer deposition method. Interestingly, the perovskite absorber reveals an improved morphology after lamination that benefits device performance. Particularly promising are the improved shelf-stability of the laminated PSCs, which retain their initial efficiency after 1-year aging, while the reference PSCs degrade rapidly, and thermal stability under prolonged continuous illumination of 100 h at 80 °C. Ultimately, lamination offers numerous advantages to perovskite-based photovoltaics for future industrial application, including parallel fabrication and optimization of devices half-stacks, the possibility of direct encapsulation, and freedom in the choice of material and deposition processes.

4. Experimental Section

Device Preparation: Substrates/superstrates were patterned ITO on glass (CAS RN 50926-11-9, Lumtec), TEONEX Q65HA PEN foil (25853-85-4, DuPont Teijin Films), ITO coated PEN foil (50926-11-9, Peccell), and SHJ solar cells. The double-side polished SHJ solar cells were provided by Forschungszentrum Jülich GmbH with the following architecture: ITO (30 nm)/a-Si:H<n> layer (≈4 nm)/a-Si:H<i> (≈4 nm)/c-Si wafer <n> (280 µm)/a-Si:H<i> (≈6 nm)/a-Si:H<p> (≈12 nm)/ITO (70 nm). Optimized reference SHJ solar cells with a large active area of 4 cm^2 demonstrated PCEs around 20%. The bottom SHJ solar cells as employed for the laminated tandem solar cells were expected to show lower performance given the reduced active area (≈0.14 cm^2). All substrates and superstrates were cleaned in ultrasonic baths of acetone (67-64-1, Sigma Aldrich) and 2-propanol (67-63-0, Sigma Aldrich) for 10 min each. Oxygen plasma treatment was performed using a Femto (Diener Electronics) on the ITO/glass substrates and ITO/PEN superstrates at 100 W for 180 s and on the SHJ solar cells—n side at 30 W for 60 s.

As hole transport layer, 20 nm NiO$_x$ (11099-02-8, Kurt J. Lesker) was sputtered using a Pro Line PVD75 (Kurt J. Lesker Company) at 1 mTorr process pressure, 100 W under RF-conditions with Argon (Ar) process gas. Afterward, oxygen plasma treatment was performed at 30 W for 30 s. Subsequently, a solution of [2-(9H-carbazol-9-yl)ethyl]phosphonic acid (2PACz, 20999-38-6, TCI; 1 m) was prepared in ethanol absolute (64-17-5, VWR Chemicals) and spin-coated onto the NiO$_x$ in one step at 3000 rpm for 30 s with 1000 rpm s^{-1} acceleration rate. Samples were annealed at 100 °C for 10 min in N_2 atmosphere.

The triple-cation perovskite absorber solution $Cs_{0.1}(MA_{0.17}FA_{0.83})_{0.9}Pb(I_{0.83}Br_{0.17})_3$ was prepared according to previous work[45] with the precursors methylammonium bromide (MABr, 6876-37-5, GreatCell Solar), formamidinium iodide (FAI, 879643-71-7, GreatCell Solar), lead iodide (PbI$_2$, 10101-63-0, TCI), lead bromide (PbBr$_2$, 10031-22-8, TCI), and cesium iodide (CsI, 7789-17-5, Alfa Aesar). Two solutions were prepared: 1) FAI (1 m), PbI$_2$ (1.1 m), MABr (0.2 m), and PbBr$_2$ (0.22 m) in N,N-dimethylformamide (Sigma Aldrich, 68-12-2):dimethyl sulfoxide (DMSO, Sigma Aldrich, 67-68-5) 4:1 v:v and 2) CsI (1.5 m) in DMSO. An 88.9 µL aliquot of solution 2 was transferred into solution 1 and then spin-coated onto the hole transport layer by two following steps: 1) 1000 rpm rotation speed for 10 s and 2) 6000 rpm for 20 s, with 5000 rpm s^{-1} acceleration rate. After 10–13 s of second step, 100 µL chlorobenzene (Sigma Aldrich, 108-90-7), was released as anti-solvent on the spinning substrate. Samples were annealed at 100 °C for 60 min in N_2 atmosphere.

For opaque PSCs (≈10.5 mm^2 active area): As rear electrode, 75 nm thick gold and as double electron transport layer, 5 nm BCP (4733-39-5 Lumtec) and 20 nm fullerene C60 (99685-96-8, Sigma Aldrich) were thermally

**ADVANCED
SCIENCE NEWS**

www.advancedsciencenews.com

**ADVANCED
ENERGY
MATERIALS**

www.advenergymat.de

evaporated using Vactec Coat 320 (Angstrom Engineering) and OPTIvap (Creaphys), respectively. For the references, C60, BCP, and then Au were sequentially deposited on top of the perovskite. For laminated devices, Au, BCP, and then C60 were sequentially deposited onto the PEN foil.

For ST (≈10.5 mm²) and tandem devices (≈14 mm²): As electron transport layer, ≈35 nm (SnO$_x$, 21651-19-4, Strem), as measured on a silicon wafer, was deposited onto the ITO/PEN foils via ALD using a Picosun R-200 Advanced (Picosun) with H$_2$O as reactant and tetrakis(dimethylamido)tin(IV) (TDMASn, 1066-77-9, Strem) as precursor. The deposition was performed at 80 °C, over 300 cycles of 1.6 s TDMASn exposure, followed by 12 s Ar/N$_2$ purging and 0.1 s H$_2$O exposure followed by 16 s of Ar/N$_2$ purging. Samples were annealed at 100 °C for 60 min in N$_2$ atmosphere. In the absence of a bubbler system, an in-built boosting system was used to increase precursor concentration. Subsequently, 20 nm C60 was deposited using the previously described procedure. The back ITO electrode of the bottom silicon solar cell was coated with silver paste (Acheson 1415, Plano GmbH) after lamination.

Hot-Pressing: The lamination was performed using an in-house developed hot embossing machine.[31,80] The two independently prepared layer stacks were placed on the lower machine plate such that the perovskite and electron transport layer face each other. In addition, a teflon-coated silicon wafer was interposed between the PEN foil and the upper plate for a uniform pressure distribution. Lamination was performed in three steps of heating/lamination/cooling under N$_2$ atmosphere (see Figure S15, Supporting Information). When the temperature of 90 °C was reached, a pressure of 80 MPa was applied for 5 min. Afterward, the sample was cooled to 40 °C and the pressure was released.

Characterization: The *J–V* characteristics and MPP tracking of the devices were recorded using a Keithley 2400 Source-Measure Unit and xenon-lamp-based Oriel Sol3A solar simulator (Newport) under controlled N$_2$ atmosphere. The intensity was calibrated with a KG5-filtered and non-filtered silicon reference solar cells for PSC and tandem devices, respectively, to match the global standard AM 1.5 G spectrum with an intensity of 100 mW cm^{-2}. *J–V* curves were measured in both forward ($J_{sc} \rightarrow V_{oc}$) and backward ($V_{oc} \rightarrow J_{sc}$) directions with a scan rate of 0.6 V s^{-1}. In Figure 2 and Figure S4, Supporting Information, references and laminated PSC were measured with 5.6 mm² masks in order to allow direct comparison. The MPP tracking measurements were performed with 0.01 V voltage perturbation. The measurement temperature was controlled using a Peltier-element and a microcontroller mounted on the sample holder for heating and cooling. The EQE was measured using the PVE300 characterization system (Bentham) with 575 Hz chopping frequency and 750 ms integration time in controlled N$_2$ atmosphere. Tandem devices were additionally illuminated with an infrared LED (940 nm) to measure the perovskite top cell and a blue LED (465 nm), white light, and band-pass (335–610 nm) filter to measure the silicon bottom cell. Reflectance and transmittance measurements were performed using a LAMBDA 1050 spectrophotometer (PerkinElmer). Atomic force microscopy images were measured using a NanoWizard II (JPK Instruments AG) in intermediate contact mode. PLQY measurements were carried out inside an integrating sphere (LabSphere, 15 cm diameter) in ambient air (relative humidity < 30%). A green laser (LD-515-10MG from Roithner Lasertechnik) was directed into the sphere via a small entrance port. An optical fiber was used to collect the emission from the exit port of the sphere and guide it to the spectrometers (AvaSpec-ULS2048 × 64TEC from Avantes). The spectral response was calibrated using a calibration lamp (HL-3plus-INT-Cal from Ocean Optics). Raw measured spectra were recalculated to give power spectra using the integration time. The PLQY was determined using the method described by de Mello et al.[81] The samples were placed at an angle of 15° with respect to the laser beam to avoid specular reflectance toward the entrance port. The implied V_{OC} (Figure 3a) was determined from the (intensity-dependent) PLQY measurements as described by Stolterfoht et al.[82] and Krueckemeier et al.[61] Photoluminescence images were acquired using the luminescence imaging setup introduced by Ternes et al.,[83] The setup was comprised of two LED bars with emission wavelength of 467nm (LDL2 by CCS Inc.) for sample excitation and a scientific

CMOS camera (Quantalux sCMOS Camera by Thorlabs) to detect the photoluminescence signal. The excitation light was filtered out with a 780 nm longpass filter (FGL780S by Thorlabs). The exposure time was set to 5s. All measurements were performed in ambient air.

Supporting Information

Supporting Information is available from the Wiley Online Library or from the author.

Conflict of Interest

The authors declare no conflict of interest.

Data Availability Statement

The data that support the findings of this study are available from the corresponding author upon reasonable request.

[1] H. Min, D. Yoon Lee, J. Kim, G. Kim, K. Su Lee, J. Kim, M. Jae Paik, Y. Ki Kim, K. S. Kim, M. Gyu Kim, T. Joo Shin, S. Il Seok, *Nature* **2021**, *598*, 444.

[2] S. D. Stranks, G. E. Eperon, G. Grancini, C. Menelaou, M. J. P. Alcocer, T. Leijtens, L. M. Herz, A. Petrozza, H. J. Snaith, *Science* **2013**, *342*, 341.

[3] Q. Dong, Y. Fang, Y. Shao, P. Mulligan, J. Qiu, L. Cao, J. Huang, *Science* **2015**, *347*, 967.

[4] S. De Wolf, J. Holovsky, S. J. Moon, P. Löper, B. Niesen, M. Ledinsky, F. J. Haug, J. H. Yum, C. Ballif, *J. Phys. Chem. Lett.* **2014**, *5*, 1035.

[5] B. Abdollahi Nejand, I. M. Hossain, M. Jakoby, S. Moghadamzadeh, T. Abzieher, S. Gharibzadeh, J. A. Schwenzer, P. Nazari, F. Schackmar, D. Hauschild, L. Weinhardt, U. Lemmer, B. S. Richards, I. A. Howard, U. W. Paetzold, *Adv. Energy Mater.* **2020**, *10*, 1902583.

[6] M. C. Tang, H. X. Dang, S. Lee, D. Barrit, R. Munir, K. Wang, R. Li, D. M. Smilgies, S. De Wolf, D. Y. Kim, T. D. Anthopoulos, A. Amassian, *Sol. RRL* **2021**, *5*, 2000718.

[7] K. A. Bush, K. Frohna, R. Prasanna, R. E. Beal, T. Leijtens, S. A. Swifter, M. D. McGehee, *ACS Energy Lett.* **2018**, *3*, 428.

[8] S. Gharibzadeh, I. M. Hossain, P. Fassl, B. A. Nejand, T. Abzieher, M. Schultes, E. Ahlswede, P. Jackson, M. Powalla, S. Schäfer, M. Rienäcker, T. Wietler, R. Peibst, U. Lemmer, B. S. Richards, U. W. Paetzold, *Adv. Funct. Mater.* **2020**, *30*, 1909919.

[9] J. Werner, B. Niesen, C. Ballif, *Adv. Mater. Interfaces* **2018**, *5*, 1700731.

[10] B. Chen, N. Ren, Y. Li, L. Yan, S. Mazumdar, Y. Zhao, X. Zhang, *Adv. Energy Mater.* **2022**, *12*, 2003628.

[11] K. Yoshikawa, H. Kawasaki, W. Yoshida, T. Irie, K. Konishi, K. Nakano, T. Uto, D. Adachi, M. Kanematsu, H. Uzu, K. Yamamoto, *Nat. Energy* **2017**, *2*, 17032.

[12] NREL Best Research-Cell Efficiency Chart, https://www.nrel.gov/pv/cell-efficiency.html (accessed: March 2022).

[13] S. E. Sofia, H. Wang, A. Bruno, J. L. Cruz-Campa, T. Buonassisi, I. M. Peters, *Sustainable Energy Fuels* **2020**, *4*, 852.

[14] A. Al-Ashouri, E. Köhnen, B. Li, A. Magomedov, H. Hempel, P. Caprioglio, J. A. Márquez, A. B. M. Vilches, E. Kasparavicius, J. A. Smith, N. Phung, D. Menzel, M. Grischek, L. Kegelmann, D. Skroblin, C. Gollwitzer, T. Malinauskas, M. Jošt, G. Matič, B. Rech, R. Schlatmann, M. Topič, L. Korte, A. Abate, B. Stannowski, D. Neher, M. Stolterfoht, T. Unold, V. Getautis, S. Albrecht, *Science (80-.).* **2020**, *370*, 1300.

[15] S. Albrecht, M. Saliba, J. P. Correa-Baena, K. Jäger, L. Korte, A. Hagfeldt, M. Grätzel, B. Rech, *J. Opt.* **2016**, *18*, 064012.

[16] E. Köhnen, P. Wagner, F. Lang, A. Cruz, B. Li, M. Roß, M. Jošt, A. B. Morales-Vilches, M. Topič, M. Stolterfoht, D. Neher, L. Korte, B. Rech, R. Schlatmann, B. Stannowski, S. Albrecht, *Sol. RRL* **2021**, *5*, 2100244.

[17] J. A. Raiford, R. A. Belisle, K. A. Bush, R. Prasanna, A. F. Palmstrom, M. D. McGehee, S. F. Bent, *Sustainable Energy Fuels* **2019**, *3*, 1517.

[18] Y. Jiang, I. Almansouri, S. Huang, T. Young, Y. Li, Y. Peng, Q. Hou, L. Spiccia, U. Bach, Y. B. Cheng, M. A. Green, A. Ho-Baillie, *J. Mater. Chem. C* **2016**, *4*, 5679.

[19] E. Aydin, J. Liu, E. Ugur, R. Azmi, G. T. Harrison, Y. Hou, B. Chen, S. Zhumagali, M. De Bastiani, M. Wang, W. Raja, T. G. Allen, A. ur Rehman, A. S. Subbiah, M. Babics, A. Babayigit, F. H. Isikgor, K. Wang, E. Van Kerschaver, L. Tsetseris, E. H. Sargent, F. Laquai, S. De Wolf, *Energy Environ. Sci.* **2021**, *14*, 4377.

[20] F. Lang, E. Köhnen, J. Warby, K. Xu, M. Grischek, P. Wagner, D. Neher, L. Korte, S. Albrecht, M. Stolterfoht, *ACS Energy Lett.* **2021**, *6*, 43.

[21] K. A. Bush, S. Manzoor, K. Frohna, Z. J. Yu, J. A. Raiford, A. F. Palmstrom, H. P. Wang, R. Prasanna, S. F. Bent, Z. C. Holman, M. D. McGehee, *ACS Energy Lett.* **2018**, *3*, 2173.

[22] K. Liu, B. Chen, Z. J. Yu, Y. Wu, Z. Huang, X. Jia, C. Li, D. Spronk, Z. Wang, Z. Wang, S. Qu, Z. C. Holman, J. Huang, *J. Mater. Chem. A* **2022**, *10*, 1343.

[23] C. Battaglia, A. Cuevas, S. De Wolf, *Energy Environ. Sci.* **2016**, *9*, 1552.

[24] S. P. Dunfield, D. T. Moore, T. R. Klein, D. M. Fabian, J. A. Christians, A. G. Dixon, B. Dou, S. Ardo, M. C. Beard, S. E. Shaheen, J. J. Berry, M. F. A. M. Van Hest, *ACS Energy Lett.* **2018**, *3*, 1192.

[25] W. Chi, S. K. Banerjee, *Chem. Mater.* **2021**, *33*, 1540.

[26] P. P. Rajbhandari, T. P. Dhakal, *J. Vac. Sci. Technol., A* **2020**, *38*, 032406.

[27] K. O. Brinkmann, T. Gahlmann, T. Riedl, *Sol. RRL* **2020**, *4*, 1900332.

[28] T. Li, W. A. Dunlap-Shohl, D. B. Mitzi, *ACS Appl. Energy Mater.* **2020**, *3*, 9493.

[29] Y. Shao, C. Zhang, S. Wang, Y. Yan, Y. Feng, J. Bian, Y. Shi, *Adv. Mater. Interfaces* **2019**, *6*, 1900157.

[30] R. Ishikawa, S. Watanabe, S. Yamazaki, T. Oya, N. Tsuboi, *ACS Appl. Energy Mater.* **2019**, *2*, 171.

[31] R. Schmager, J. Roger, J. A. Schwenzer, F. Schackmar, T. Abzieher, M. Malekshahi Byranvand, B. Abdollahi Nejand, M. Worgull, B. S. Richards, U. W. Paetzold, *Adv. Funct. Mater.* **2020**, *30*, 1907481.

[32] I. Y. Choi, C. U. Kim, W. Park, H. Lee, M. H. Song, K. K. Hong, S. Il Seok, K. J. Choi, *Nano Energy* **2019**, *65*, 104044.

[33] J. H. Heo, Y. K. Choi, C. W. Koh, H. Y. Woo, S. H. Im, *Adv. Mater. Technol.* **2019**, *4*, 1800390.

[34] D. Bryant, P. Greenwood, J. Troughton, M. Wijdekop, M. Carnie, M. Davies, K. Wojciechowski, H. J. Snaith, T. Watson, D. Worsley, *Adv. Mater.* **2014**, *26*, 7499.

[35] H. Zhang, R. Liu, S. Guo, Z. Wang, X. Sun, J. Lin, Q. Luo, C. Q. Ma, *Org. Electron.* **2022**, *100*, 106352.

[36] X. L. Trinh, H. C. Kim, *Energy Rep.* **2020**, *6*, 1297.

[37] H. Zhang, Y. Zhang, G. Yang, Z. Ren, W. Yu, D. Shen, C. S. Lee, Z. Zheng, G. Li, *Sci. China: Chem.* **2019**, *62*, 875.

[38] T. R. Klein, B. G. Lee, M. Schnabel, E. L. Warren, P. Stradins, A. C. Tamboli, M. F. A. M. Van Hest, *ACS Appl. Mater. Interfaces* **2018**, *10*, 8086.

[39] W. A. Dunlap-Shohl, T. Li, D. B. Mitzi, *ACS Appl. Energy Mater.* **2019**, *2*, 5083.

[40] C. O. Ramírez Quiroz, G. D. Spyropoulos, M. Salvador, L. M. Roch, M. Berlinghof, J. Darío Perea, K. Forberich, L. Dion-Bertrand, N. J. Schrenker, A. Classen, N. Gasparini, G. Chistiakova, M. Mews, L. Korte, B. Rech, N. Li, F. Hauke, E. Spiecker, T. Ameri, S. Albrecht, G. Abellán, S. León, T. Unruh, A. Hirsch, A. Aspuru-Guzik, C. J. Brabec, *Adv. Funct. Mater.* **2019**, *29*, 1901476.

[41] E. Lamanna, F. Matteocci, E. Calabrò, L. Serenelli, E. Salza, L. Martini, F. Menchini, M. Izzi, A. Agresti, S. Pescetelli, S. Bellani, A. E. Del Río Castillo, F. Bonaccorso, M. Tucci, A. Di Carlo, *Joule* **2020**, *4*, 865.

[42] H. Kanda, A. Uzum, H. Nishino, T. Umeyama, H. Imahori, Y. Ishikawa, Y. Uraoka, S. Ito, *ACS Appl. Mater. Interfaces* **2016**, *8*, 33553.

[43] Y. Yang, Y. Zhu, X. Wang, Q. Song, C. Ji, H. Zhang, Z. He, C. Liang, *Int. J. Photoenergy* **2020**, *2020*, 5039192.

[44] B. Ding, J. Peng, Q.-Q. Chu, S. Zhao, H. Shen, K. J. Weber, G.-J. Yang, T. P. White, K. R. Catchpole, M. K. Nazeeruddin, P. J. Dyson, *Sol. RRL* **2021**, *5*, 2000729.

[45] M. Saliba, T. Matsui, J. Y. Seo, K. Domanski, J. P. Correa-Baena, M. K. Nazeeruddin, S. M. Zakeeruddin, W. Tress, A. Abate, A. Hagfeldt, M. Grätzel, *Energy Environ. Sci.* **2016**, *9*, 1989.

[46] E. Lamanna, F. Matteocci, E. Calabrò, L. Serenelli, E. Salza, L. Martini, F. Menchini, M. Izzi, A. Agresti, S. Pescetelli, S. Bellani, A. E. D. R. Castillo, F. Bonaccorso, M. Tucci, A. Di Carlo, *Joule* **2020**, *4*, 865.

[47] C. O. Ramírez Quiroz, G. D. Spyropoulos, M. Salvador, L. M. Roch, M. Berlinghof, J. Darío Perea, K. Forberich, L. Dion-Bertrand, N. J. Schrenker, A. Classen, N. Gasparini, G. Chistiakova, M. Mews, L. Korte, B. Rech, N. Li, F. Hauke, E. Spiecker, T. Ameri, S. Albrecht, G. Abellán, S. León, T. Unruh, A. Hirsch, A. Aspuru-Guzik, C. J. Brabec, *Adv. Funct. Mater.* **2019**, *29*, 1901476.

[48] F. Fu, J. Li, T. C. Yang, H. Liang, A. Faes, Q. Jeangros, C. Ballif, Y. Hou, *Adv. Mater.* **2022**, 2106540.

[49] Y. He, Z. Tang, L. Mao, S. Yang, T. Yang, M. Xie, Q. Chang, L. Ding, B. He, C. Peng, C. Yu, X. Hao, J. Zhang, K. Zheng, C. Han, Y. Zhang, H. Yan, X. Xu, *Phys. Status Solidi RRL* **2021**, *15*, 2100119.

[50] F. Sahli, J. Werner, B. A. Kamino, M. Bräuninger, T. C. J. Yang, P. Fiala, G. Nogay, F. Fu, R. Monnard, A. Walter, S. J. Moon, E. Rucavado, L. Barraud, B. Paviet-Salomon, C. Allebe, L. Ding, J. J. D. Leon, D. Sacchetto, G. Cattaneo, M. Morales-Masis, M. Boccard, M. Despeisse, S. Nicolay, Q. Jeangros, B. Niesen, C. Ballif, 2018 IEEE 7th World Conf. Photovoltaic Energy Conversion, IEEE, Piscataway **2018**, p. 3571.

[51] M. Schultes, T. Helder, E. Ahlswede, M. F. Aygüler, P. Jackson, S. Paetel, J. A. Schwenzer, I. M. Hossain, U. W. Paetzold, M. Powalla, *ACS Appl. Energy Mater.* **2019**, *2*, 7823.

[52] F. Sahli, J. Werner, B. A. Kamino, M. Bräuninger, R. Monnard, B. Paviet-Salomon, L. Barraud, L. Ding, J. J. Diaz Leon, D. Sacchetto,

**ADVANCED
SCIENCE NEWS**

www.advancedsciencenews.com

**ADVANCED
ENERGY
MATERIALS**

www.advenergymat.de

G. Cattaneo, M. Despeisse, M. Boccard, S. Nicolay, Q. Jeangros, B. Niesen, C. Ballif, *Nat. Mater.* **2018**, *17*, 820.

[53] S. Manzoor, Z. J. Yu, A. Ali, W. Ali, K. A. Bush, A. F. Palmstrom, S. F. Bent, M. D. McGehee, Z. C. Holman, *Sol. Energy Mater. Sol. Cells* **2017**, *173*, 59.

[54] Y. Hou, E. Aydin, M. De Bastiani, C. Xiao, F. H. Isikgor, D. J. Xue, B. Chen, H. Chen, B. Bahrami, A. H. Chowdhury, A. Johnston, S. W. Baek, Z. Huang, M. Wei, Y. Dong, J. Troughton, R. Jalmood, A. J. Mirabelli, T. G. Allen, E. Van Kerschaver, M. I. Saidaminov, D. Baran, Q. Qiao, K. Zhu, S. De Wolf, E. H. Sargent, *Science* **2020**, *367*, 1135.

[55] B. Chen, Z. J. Yu, S. Manzoor, S. Wang, W. Weigand, Z. Yu, G. Yang, Z. Ni, X. Dai, Z. C. Holman, J. Huang, *Joule* **2020**, *4*, 850.

[56] J. Wang, C. Gao, X. Wang, Y. Wang, Z. Cheng, H. Liu, W. Shen, *Energy Technol.* **2021**, *9*, 2000778.

[57] M. De Bastiani, A. J. Mirabelli, Y. Hou, F. Gota, E. Aydin, T. G. Allen, J. Troughton, A. S. Subbiah, F. H. Isikgor, J. Liu, L. Xu, B. Chen, E. Van Kerschaver, D. Baran, B. Fraboni, M. F. Salvador, U. W. Paetzold, E. H. Sargent, S. De Wolf, *Nat. Energy* **2021**, *6*, 167.

[58] P. Tockhorn, J. Sutter, A. Cruz, P. Wagner, K. Jaeger, D. Yoo, F. Lang, M. Grischek, B. Li, A. Al-Ashouri, E. Koehnen, M. Stolterfoht, D. Neher, R. Schlatmann, B. Rech, B. Stannowski, S. Albrecht, C. Becker, (Preprint) https://doi.org/10.21203/rs.3.rs-1439562/v1 submitted March 2022.

[59] F. Gota, M. Langenhorst, R. Schmager, J. Lehr, U. W. Paetzold, *Joule* **2020**, *4*, 2387.

[60] M. Singh, R. Santbergen, I. Syifai, A. Weeber, M. Zeman, O. Isabella, *Nanophotonics* **2021**, *10*, 2043.

[61] L. Krückemeier, U. Rau, M. Stolterfoht, T. Kirchartz, *Adv. Energy Mater.* **2020**, *10*, 1902573.

[62] K. Datta, J. Wang, D. Zhang, V. Zardetto, W. H. M. Remmerswaal, C. H. L. Weijtens, M. M. Wienk, R. A. J. Janssen, *Adv. Mater.* **2022**, *34*, 2110053.

[63] T. Todorov, T. Gershon, O. Gunawan, Y. S. Lee, C. Sturdevant, L. Y. Chang, S. Guha, *Adv. Energy Mater.* **2015**, *5*, 1500799.

[64] M. Langenhorst, B. Sautter, R. Schmager, J. Lehr, E. Ahlswede, M. Powalla, U. Lemmer, B. S. Richards, U. W. Paetzold, *Prog. Photovoltaics* **2019**, *27*, 290.

[65] S. Gharibzadeh, P. Fassl, I. M. Hossain, P. Rohrbeck, M. Frericks, M. Schmidt, T. Duong, M. R. Khan, T. Abzieher, B. A. Nejand, F. Schackmar, O. Almora, T. Feeney, R. Singh, D. Fuchs, U. Lemmer, J. P. Hofmann, S. A. L. Weber, U. W. Paetzold, *Energy Environ. Sci.* **2021**, *14*, 5875.

[66] N. Thongprong, T. Supasai, Y. Li, I. M. Tang, N. Rujisamphan, *Energy Technol.* **2020**, *8*, 1901196.

[67] T. S. Sherkar, C. Momblona, L. Gil-Escrig, J. Ávila, M. Sessolo, H. J. Bolink, L. J. A. Koster, *ACS Energy Lett.* **2017**, *2*, 1214.

[68] Zhanfei Zhang, Jianli Wang, Lizhong Lang, Yan Dong, Jianghu Liang, Yiting Zheng, Xueyun Wu, Congcong Tian, Ying Huang, Zhuang Zhou, Yajuan Yang, Luyao Wang, Lingti Kong, Chun-Chao Chen, *J. Mater. Chem. A* **2022**, *10*, 3605.

[69] H. Amrollahi Bioki, A. Moshaii, M. Borhani Zarandi, *Synth. Met.* **2022**, *283*, 116965.

[70] S. Sidhik, A. C. Pasarán, C. Rosiles Pérez, T. López-Luke, E. De La Rosa, *J. Mater. Chem. C* **2018**, *6*, 7880.

[71] S. Wang, Z. Ma, Z. Liu, W. Wu, Y. Zhu, R. Ma, C. Wang, *Sol. RRL* **2018**, *2*, 1800034.

[72] X. Li, X. Tang, T. Ye, D. Wu, H. Wang, X. Wang, *ACS Appl. Mater. Interfaces* **2017**, *9*, 18730.

[73] Y. Han, S. Meyer, Y. Dkhissi, K. Weber, J. M. Pringle, U. Bach, L. Spiccia, Y.-B. Cheng, *J. Mater. Chem. A* **2015**, *3*, 8139.

[74] R. A. Kerner, L. Zhao, S. P. Harvey, J. J. Berry, J. Schwartz, B. P. Rand, *ACS Energy Lett.* **2020**, *5*, 3352.

[75] S. Cacovich, L. Ciná, F. Matteocci, G. Divitini, P. A. Midgley, A. Di Carlo, C. Ducati, *Nanoscale* **2017**, *9*, 4700.

[76] N. N. Shlenskaya, N. A. Belich, M. Grätzel, E. A. Goodilin, A. B. Tarasov, *J. Mater. Chem. A* **2018**, *6*, 1780.

[77] C. Besleaga, L. E. Abramiuc, V. Stancu, A. G. Tomulescu, M. Sima, L. Trinca, N. Plugaru, L. Pintilie, G. A. Nemnes, M. Iliescu, H. G. Svavarsson, A. Manolescu, I. Pintilie, *J. Phys. Chem. Lett.* **2016**, *7*, 5168.

[78] L. Shi, M. P. Bucknall, T. L. Young, M. Zhang, L. Hu, J. Bing, D. S. Lee, J. Kim, T. Wu, N. Takamure, D. R. McKenzie, S. Huang, M. A. Green, A. W. Y. Ho-Baillie, *Science* **2020**, *368*, eaba2412.

[79] E. J. Juarez-Perez, L. K. Ono, M. Maeda, Y. Jiang, Z. Hawash, Y. Qi, *J. Mater. Chem. A* **2018**, *6*, 9604.

[80] M. Worgull, *Hot Embossing, Theory and Technology of Microreplication*, Elsevier Inc, Amsterdam **2009**.

[81] J. C. de Mello, H. F. Wittmann, R. H. Friend, *Adv. Mater.* **1997**, *9*, 230.

[82] M. Stolterfoht, M. Grischek, P. Caprioglio, C. M. Wolff, E. Gutierrez-Partida, F. Peña-Camargo, D. Rothhardt, S. Zhang, M. Raoufi, J. Wolansky, M. Abdi-Jalebi, S. D. Stranks, S. Albrecht, T. Kirchartz, D. Neher, *Adv. Mater.* **2020**, *32*, 2000080.

[83] S. Ternes, F. Laufer, P. Scharfer, W. Schabel, B. S. Richards, I. A. Howard, U. W. Paetzold, *Sol. RRL* **2022**, *6*, 2100353.

2200961 (10 of 10)